

Veröffentlichung

Im Rahmen des SFB 880. www.sfb880.tu-braunschweig.de

Autoren

Burnazzi, Marco;Radespiel, Rolf

Titel

Design and Analysis of a Droop Nose for Coanda Flap Applications

Publisher o. Konferenz

AIAA JOURNAL OF AIRCRAFT Vol. 51, No. 5, DOI: 10.2514/1.C032434

Jahr

2014

Internet-Link (Doi-Nr.)

<http://arc.aiaa.org/doi/abs/10.2514/1.C032434>

Design and Analysis of a Droop Nose for Coanda Flap Applications

Marco Burnazzi* and Rolf Radespiel†

Technische Universität Braunschweig, 38108 Brunswick, Germany

DOI: 10.2514/1.C032434

The present study describes the fundamentals of droop nose design for improving the aerodynamics of airfoils with active high-lift using an internally blown Coanda-type flap. The main objectives are to increase the stall angle of attack and reduce the power required by the high-lift system. A two-dimensional sensitivity analysis explores the effects of varying airfoil camber and thickness in the first 20% of the chord. The resulting droop nose configuration improves the maximum lift coefficient by about 20% and increases the stall angle of attack by around 10–15 deg. A target lift coefficient of about 4.7 is reached with 28% less jet momentum coefficient, compared to the clean nose. As the modified leading-edge geometry presents different stall mechanisms, the aerodynamic response to variations of jet momentum is also different. In particular, for a jet momentum coefficient above 0.035, the stall angle of attack increases with jet momentum, in contrast with the behavior observed with the clean nose.

Nomenclature

$C_{d_{stall}}$	=	stall drag coefficient
$C_{l_{max}}$	=	maximum lift coefficient
$C_{m_{stall}}$	=	stall pitching moment coefficient
C_p	=	pressure coefficient
C_μ	=	momentum coefficient of the Coanda jet
c	=	airfoil chord
h	=	local distance from the wall
L_f	=	flap length
L_n	=	nose length
M	=	Mach number
\dot{m}_j	=	mass flow rate of the Coanda jet
Re	=	Reynolds number
S_{ref}	=	reference surface
th_{le}	=	thickness factor at the leading edge
v	=	local absolute velocity
v_∞	=	far-field velocity
v_j	=	averaged velocity of the jet through the plenum exit section
α	=	angle of attack
α_{stall}	=	stall angle of attack
β	=	camber line angle at the leading edge, due to a rigid deflection of the nose
γ	=	camber line angle at the leading edge, due to a smooth camber increase of the nose
δ	=	flap deflection angle
δ_2	=	momentum thickness of the boundary layer
ρ_∞	=	far-field density

I. Introduction

THE development of the civil air transport is more and more affected by the limited number of airports for long- and medium-range aircraft. In a few years, many existing airport infrastructures will reach their maximum capacity, and this could limit further growth of air transport. On the other hand, many small airports are not in use for commercial transport because of short runways and their

proximity to populated areas. These hurdles may be overcome by introducing a new class of short- to medium-range transport aircraft, which represents a competitive alternative to the widely used B737, A320, and similar aircraft. Such new airplanes must have short takeoff and landing capabilities and very low noise emissions in order to allow operations from smaller and close-to-city airports. The high-lift systems of these aircraft are the key to their flight performance, as they facilitate an aircraft with both high wing loading and low flight speeds at takeoff and landing, thereby reducing runway length and airframe noise.

The present work is part of the Collaborative Research Center SFB880 (Sonderforschungsbereich 880) (hereafter referred to as Center) located at Technische Universität Braunschweig (Technical University in Brunswick) in Germany. The Center aims at new technologies that satisfy the aforementioned high-lift requirements. Fundamentals in aeroacoustic, active high-lift technologies and flight dynamics are addressed.

One particular aim is to obtain drastic enhancement of lift coefficients in a way suited for transport aircraft applications. Here, we follow the research hypothesis that this can be accomplished by employing aerodynamic configurations where the lift is augmented by well-designed blowing. The concept of wing blowing to improve lift has been known since the late 1920s [1]. Numerous powered-lift concepts have been explored since, see [2]. Externally blown high-lift configurations use the propulsive jet of the aircraft engine to achieve a lift increase. The resulting concepts are referred to as “vectored slipstream” for propeller aircraft, “externally blown flaps” for jet engines mounted close to the lower wing surface, and “upper surface blowing” for the jet engine located above the wing. These approaches have the potential of medium-powered lift coefficients achievable for a given thrust-to-weight ratio [3]. Higher-powered lift augmentation may be obtained by using internal blowing, such as blowing over Coanda surfaces close to the trailing edge. This approach uses the entrainment capabilities of a tangentially blown wall jet in order to keep the flow attached to the blunt, rounded trailing edge. This allows a direct control of the flow angle close to the trailing edge, and hence circulation control. Englar [4] gives a comprehensive review of research work on this concept. With a blunt trailing edge, one needs some blowing at cruise condition in order to obtain low drag [4,5], but this is not a viable solution for transport aircraft. The alternative is to install a movable flap at the trailing edge that generates the Coanda surface during takeoff and landing only. A good example is Englar’s dual-radius flap [4], designed to generate near-optimum Coanda shapes [6]. Englar’s configuration represents a specially designed internally blown flap. Internally blown flaps may hence be viewed as a special case of circulation control since they use the Coanda effect at their curved leading edge if large turning angles are to be accomplished, as seen in Fig. 1. Therefore, they are called Coanda flaps.

The aerodynamic developments previously described were merely led by wind-tunnel experiments. Numerical flow simulation offers

Presented as Paper 2013-487 at the 51st AIAA Aerospace Sciences Meeting Including the New Horizons Forum and Aerospace Exposition, Grapevine, TX, 7–10 January 2013; received 16 May 2013; revision received 12 December 2013; accepted for publication 6 January 2014; published online 16 May 2014. Copyright © 2013 by Burnazzi Marco. Published by the American Institute of Aeronautics and Astronautics, Inc., with permission. Copies of this paper may be made for personal or internal use, on condition that the copier pay the \$10.00 per-copy fee to the Copyright Clearance Center, Inc., 222 Rosewood Drive, Danvers, MA 01923; include the code 1542-3868/14 and \$10.00 in correspondence with the CCC.

*Research Assistant, Institute of Fluid Mechanics. Student Member AIAA.

†Professor and Head of Institute, Institute of Fluid Mechanics. Senior Member AIAA.

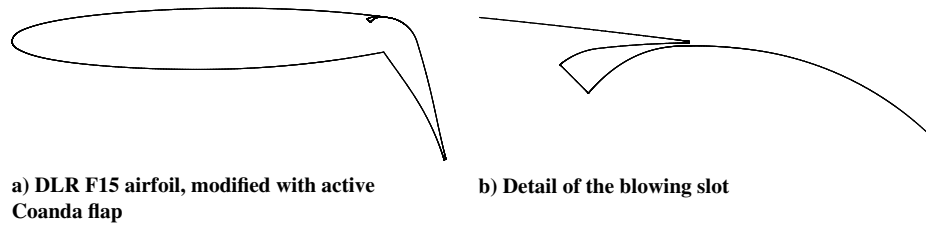


Fig. 1 Transonic airfoil with high-lift flap set at $\delta = 65$ deg.

new opportunities to the development of efficient lift augmentation systems by taking advantage of detailed flow analyses not possible using experimental data [7]. Technische Universität Braunschweig used numerical flow simulations to analyze design sensitivities of internally blown flaps with respect to flap geometry, flap settings, blowing slot, and blowing rates [8–10]. The aim of the work was to design a flap arrangement capable of achieving high-lift gains with low blowing momentum, as required by overall transport aircraft design considerations.

The present aerodynamic research extends the design space to the overall shape of the airfoil. Again, the primary objective is to obtain high-lift coefficients at low-power consumption of the blowing system. The research is guided by the following design choices:

1) The concept of active circulation control using internally blown flaps yields large lift gains, and it can be adapted to different operation points by flap setting;

2) Any trailing-edge and leading-edge devices should function without slots, because slot flows are major sources of airframe noise [11].

The mechanical complexity of the internally blown flap may be kept at a reasonable level by moving the flap around a simple hinge. Figure 1 shows the 65 deg flap setting used in the present study and the shape of the blowing slot.

The efficiency of the active circulation control device is represented by the lift gain factor, defined as the ratio between the increase of maximum lift coefficient due to the active circulation control system and the jet momentum coefficient needed to obtain this gain. The increase of lift is referred to the maximum lift coefficient of the airfoil with a deflected flap and without blowing: $C_{l_{\max}} = 2.314$ in the present study. The jet momentum coefficient is given by

$$C_{\mu} = \frac{v_j \dot{m}_j}{(1/2)\rho_{\infty} v_{\infty}^2 S_{\text{ref}}} \quad (1)$$

The present paper presents significant improvements of the airfoil shape to obtain high lift gain factors. Section II briefly describes the status of the Coanda flap designed in previous works using a fixed geometry of leading edge and wingbox. It appears that very high circulation due to high flap deflection angles introduces the need of a leading-edge device in order to avoid local separation at the leading edge. Following the guideline to avoid a slot, a fixed percentage of the chord length (that is the part of the airfoil not occupied by the wingbox) is then modified in order to obtain a droop nose configuration. Such a device allows reduction of the suction peak at the leading edge caused by the high circulation due to the active trailing-edge device, thereby increasing the stall angle of attack. Shmilovich and Yadlin compared a rigid droop nose device that rotated around a hinge line and a conventional slat in combination with an active high-lift flap with boundary-layer control [12]. Their slat configuration yields a higher stall angle compared to the droop nose [12]. They also discussed the complexity of flow interactions generated by a slotted device [13]. For instance, the viscous slat wake exhibits a sudden spreading as it is exposed to a strong adverse pressure gradient along the flap. Such interactions can limit maximum lift, even without boundary-layer separation from the airfoil surface [14].

An optimization approach for a droop nose bending around a hinge line and a comparison of the resulting geometry with a Krueger flap are presented by Jirásek and Amoignon in [15]. Kintscher et al. [16]

and Wild [17] studied the potentials of shape-adaptive droop noses in combination with a Fowler flap. Some of their results are shown in Sec. IV, where the relative performance of shape-adaptive droop noses for use with Fowler flaps and Coanda flaps are compared.

The leading-edge shape described in the present paper is intended for landing and takeoff operations. Therefore, an elastic skin and a suited internal structure are needed for morphing the shape. The main aerodynamic design steps that brought out the currently most effective shape are described. As a result, this leading edge shows impressing improvements of blowing efficiency, and hence its suitability for applications in commercial transport aircraft. Finally, the stall behavior of the airfoil equipped with the droop nose and its dependence on blowing momentum are compared with the case without a leading-edge device. This yields physical insight into the viscous losses in active high-lift systems and into particular stalling mechanisms not known before.

II. Previous Studies

Previous numerical and experimental flow research at Technische Universität Braunschweig has contributed to the aerodynamic design experience in Coanda flaps. Design sensitivity studies led to the selection of particular flap configurations, and these were thoroughly analyzed in [8–10]. The most important design parameters are flap deflection angle, momentum coefficient, and blowing slot height. Whereas flap angle and blowing momentum coefficient should increase for increased lift targets, optimal slot heights are rather low, with values of around 0.0006 airfoil chord lengths, and mostly independent of the flap angle. The curvature value of the Coanda surface used as a flap knuckle shape is less important. A radius of curvature of around 0.07 chord lengths is a reasonable choice. Also, a flap length suited to achieve high-lift gains could be identified. Good values are 0.25–0.30 of the airfoil chord. With these design choices, and assuming steady wall jet blowing, typical lift gains over a blowing momentum (“lift gain factor,” as defined in Sec. I) of 66 were obtained at a lift coefficient of around 4 and with a flap deflection angle of 50 deg, whereas this value was reduced to 48 at a lift coefficient of around 6 and $\delta = 80$ deg (analyses conducted with $Re = 20 \cdot 10^6$). It was noticed that the angle of attack of maximum lift decreases for higher blowing rates, as seen in Fig. 2. This indicates that viscous losses due to the suction peak at the nose grow rapidly with blowing rate and alpha. Leading-edge separation always occurred for lift coefficients above 6.

Local blowing from a carefully designed slot at the nose or at other locations of the airfoil did not help much, as it removed the separation but also led to decreased lift gain factors. Such solutions have been thoroughly analyzed, both numerically and experimentally, by Englar et al., as described in [18]. The results indicate the need for very high blowing rates at the leading-edge blowing slot.

The present work aims at solving the observed problems that could prevent Coanda flap configurations from being employed for practical applications. In particular, the main objectives are 1) further reduction of the power required by the high-lift device (that is, reduction of C_{μ}); and 2) increase of the stall angle of attack to values suitable for applications on aircraft.

III. Numerical Setup

The present droop nose investigations are based on two-dimensional (2-D) flow simulations of the DLR-F15 airfoil, developed by the

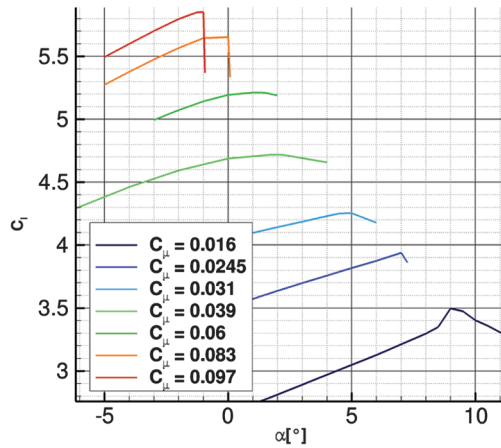


Fig. 2 Effect of the jet momentum on the stall angle of attack (flap deflection $\delta = 65$ deg, $Re = 12 \cdot 10^6$, and $M = 0.15$).

German Aerospace Research Center (DLR), with different nose shapes. The computational fluid dynamics (CFD) solver employed to perform the analysis is the DLR TAU-Code [19,20]. The Reynolds-averaged Navier–Stokes (RANS) equations are solved by using a finite volume approach. The discretization scheme, turbulence model, and other numerical parameters have been previously assessed by means of wind-tunnel experiments [21,22]. In particular, the following results and analyses are obtained by a second-order central scheme for the mean-flow inviscid flux and a second-order upwind Roe scheme for the advection term of the turbulence equation. The turbulence model is Spalart–Allmaras with a correction due to flow rotation and curvature [23]. This last module improves the physical modeling of the one-equation turbulence model in regions where the streamlines have a high curvature. This characteristic is very important for the simulation of the Coanda phenomenon, which is based on the equilibrium between the inertia forces and the momentum transport in the direction normal to the convex surface [10].

Due to the large number of simulations required by the present analysis, the number of grid points was set by means of a mesh convergence exercise, based on Richardson extrapolation [24]. This

procedure provides an estimation of the spatial discretization error and of the minimum number of points that ensures an acceptable accuracy. Three grids were tested, which contained around 70,000, 230,000, and 920,000 points. The corresponding maximum lift coefficients of 4.410, 4.456, and 4.480 were obtained for all the grids at $\alpha = 3.0$ deg. Based on these values, the Richardson extrapolation yields a value of the maximum lift coefficient of 4.496, which is an approximation of using an infinite large number of grid points. This value is used as a reference value to determine the grid resolution error, which is 1.91, 0.89, and 0.36% for the three grids, respectively.

The grid chosen for the flow analyses discussed in the present work represents a compromise between accuracy and computational cost. This is the medium grid, with about 230,000 points. The grid is composed by an unstructured region and a structured area. The structured grid layer is employed to cover the region where relevant viscous phenomena occur. Its y^+ values of the first grid layer close to the wall are always less than one. Figure 3 displays some of the main features of the mesh. An important characteristic of the grid is the density of points along the pressure side, as the stagnation point is located far downstream of the leading edge, for large angles of attack. Therefore, an overall large amount of points is necessary to properly capture the flow attachment. The structured region is extended over a large area around the flap, in order to capture vortical flow, as expected in case of flow separation from the flap. Both the trailing edge and the edge of the slot lip are discretized by means of a local C-block topology in order to avoid the propagation of high-point density in areas where grid points are not needed and might slow down the convergence (Fig. 3d).

IV. Evolution of the Geometry

The geometrical leading-edge parameters in the present work have been chosen in order to provide sufficient degrees of freedom but also to ensure a low number of parameters for observation of engineering sensitivities. An important constraint from nose structure considerations determines the skin length of the modified surface that must be equal to the length of the original airfoil. The search for an effective shape begins with the simple deflection of the original nose shape, followed by an increase of its thickness and a progressive increase of the camber line droop. The different geometries are evaluated and compared by computing the maximum lift coefficient

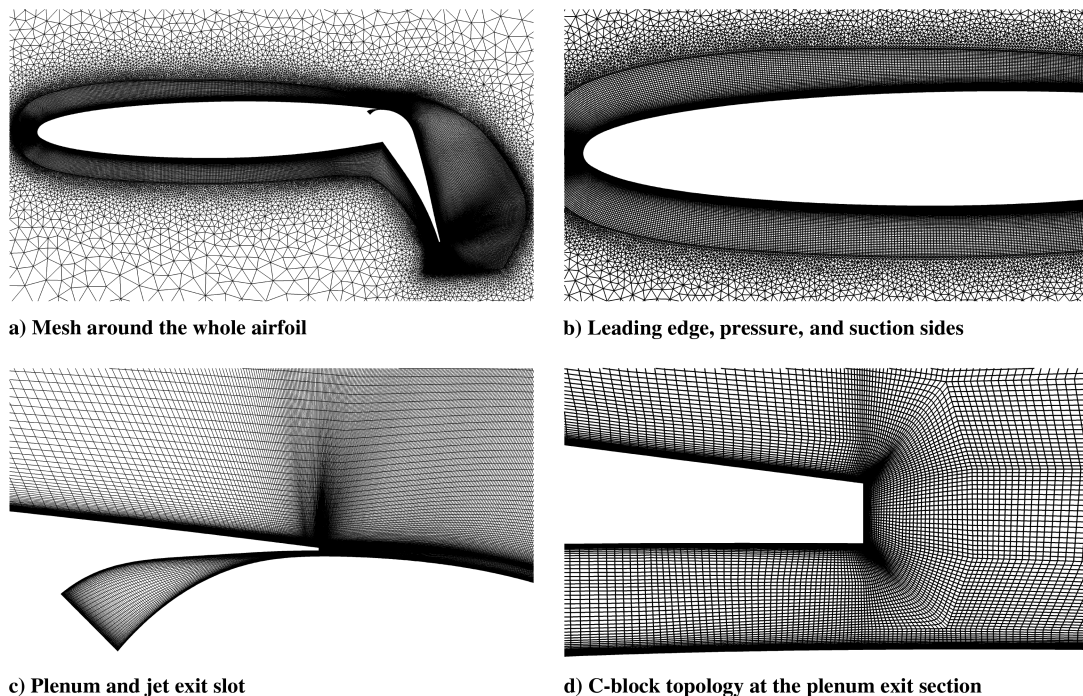


Fig. 3 Numerical hybrid grid used in the present study.

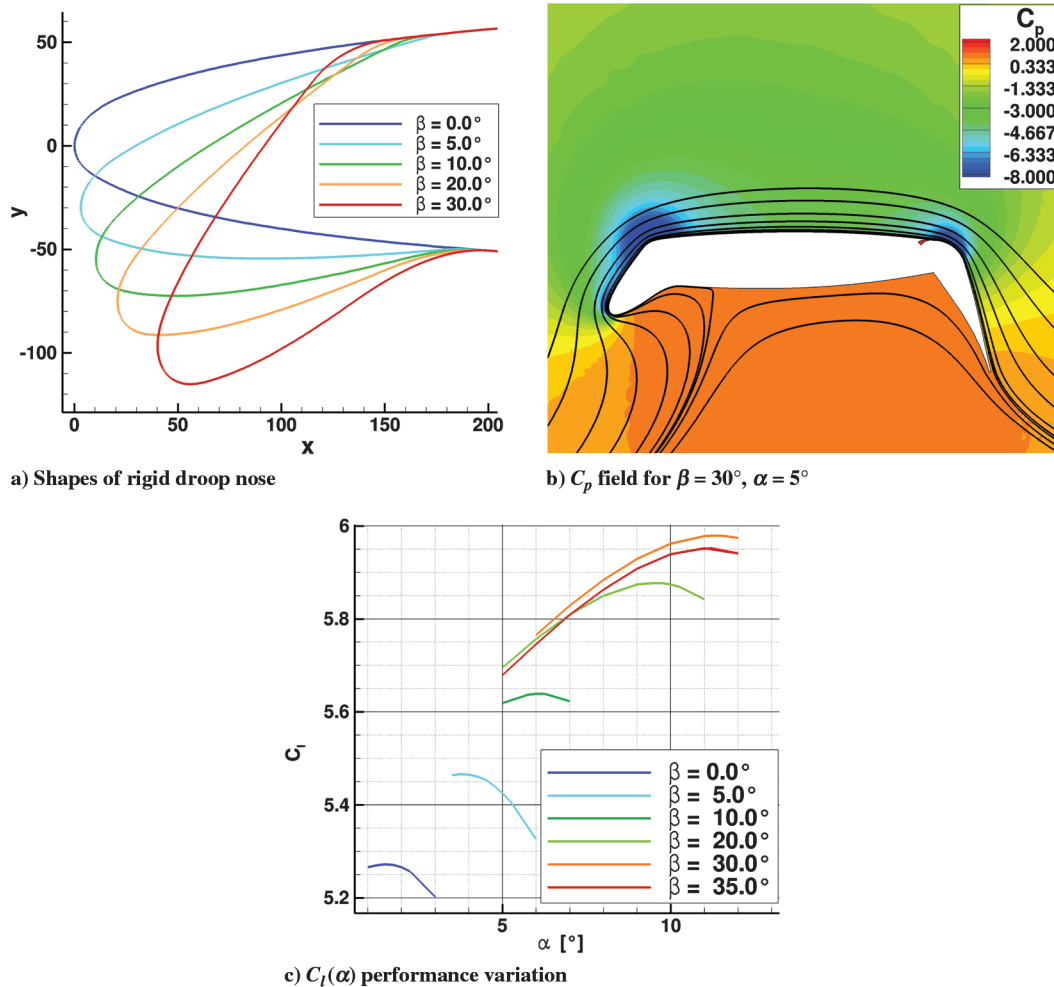


Fig. 4 Rigid droop nose shapes and behavior ($Re = 10^7$, $M = 0.15$, $C_\mu = 0.06$).

and the respective angle of attack. In this first step of the analysis, Reynolds number, Mach number, blowing momentum, flap deflection angle, and flap length are kept constant: $Re = 10^7$, $M = 0.15$, $C_\mu = 0.06$, $\delta = 65$ deg, and $L_f/c = 0.25$. The allowed length of the droop nose is fixed to $L_n/c = 0.20$.

A. Rigid Droop Nose

The first leading-edge device is obtained by deflecting the leading edge downward, without modifying its shape (Fig. 4a). Therefore, this technique does not involve structure deformation (except for the hinge-cover sheet at the lower surface) and can be achieved by a simple rotation of the nose around a hinge. Thanks to its efficiency and mechanical simplicity, this device is currently employed by some commercial transport aircraft, like the Airbus A380.

This configuration is characterized by two strong peaks of low pressure (Fig. 4b), as the deflection of the nose creates a new region of high curvature on the suction side. Nevertheless, the improvement of lift generation with respect to the clean-nose configuration is significant, as shown in Table 1 and Fig. 4c, where the deflection is expressed by the angle β . Note that the improvements in lift are larger than those known from applications in combination with mechanical high-lift flaps: in [25], a lift coefficient increment of 0.3 is assumed

for a 2-D configuration with leading-edge flap in combination with a conventional trailing-edge flap, whereas in the present case, the increment of lift coefficient is about 0.7.

B. Thickness Increase

To reduce the low-pressure peaks, the thickness of the nose is varied. The new nose geometry is obtained by multiplying the distance of each point of the contour from the camber line by a function f such that, in the connection to the wingbox (fixed part of the airfoil), it is

$$f(x_{\text{wingbox}}) = 1 \quad (2)$$

$$f'(x_{\text{wingbox}}) = 0 \quad (3)$$

A parabolic function can be used for the function f , as well as combinations of spline or trigonometric functions. The resulting thickness increase is symmetric with respect to the camber line.

According to Fig. 5a, the new thickness in a generic point x is given by

$$d_{\text{new}}(x) = d(x) \cdot f(x) \quad (4)$$

Figure 5b shows the reduction of chord length that is required to maintain the initial skin length. In the present configurations, the thickness is increased by a parabolic function using as a control parameter the value of the function f at the leading edge, $f(0) = \text{th}_{\text{le}}$. Starting from a rigid nose deflection of 10 deg, the highest

Table 1 Improvements achieved by a rigid rotation of the nose

	$C_{l_{\text{max}}}$	α_{stall} , deg
Clean nose	5.27	1.5
Rigid droop nose $\beta = 30$ deg	5.98	11.3

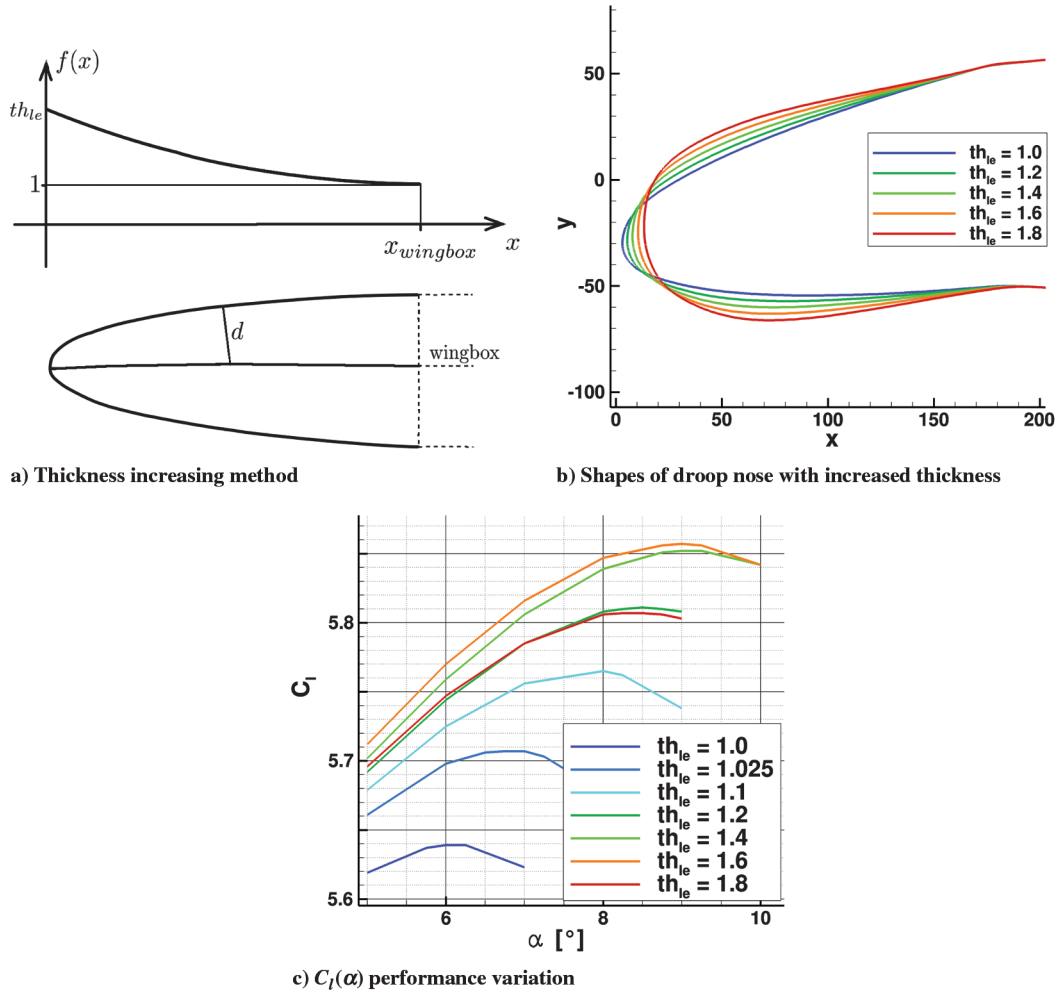


Fig. 5 Thickness increase, shapes, and performances ($Re = 10^7$, $M = 0.15$, $C_\mu = 0.06$).

performance improvement is achieved with $th_{1e} = 1.6$, which is reported in Table 2.

The thickness increase distributes the low pressure over a larger area and reduces the suction peak. Nevertheless, a too high value of function f at the leading edge creates an undesired augmentation of the surface curvature, resulting in lower performances (Fig. 5c).

C. Camber Increase

A better control of the pressure distribution along the nose is obtained by changing the camber of the mean line. The new camber is controlled by three radii of camber curvature: $x/c = 0.2, 0.1, 0.0$. However, in the present study, a constant value is used for the three radii; and the resulting angle of the mean line at the leading edge, expressed by γ , is used as parameter to describe the nose deflection. A comparison between a rigid nose deflection and a smooth camber increase is shown in Fig. 6, where the two nose-drooping methods are applied independently: either β is varied or γ . The low-pressure peak at the knee over the hinge of the rigid nose does not occur for a smooth camber line, according to Fig. 6c. In particular, for large nose

deflections, the hinge peak causes very high losses, which result in a decrease of performance; see Fig. 6b. The best result obtained by camber increase, without any thickness variation, provides the gain shown in Table 3.

D. Camber and Thickness Increase

Currently, the most effective configuration is obtained by combining an increase of thickness and camber. In this design work, the same value is given to the three radii of the camber control. That means that the camber line is a circle arc. Further studies aimed at optimizing the nose shape indicated very little potential of using curvature variations towards the leading edge. In Fig. 7 one can see a comparison between the clean-nose configuration and the currently best droop nose design. The distributions of the pressure coefficient represent stall conditions, and the resulting lift coefficients are shown in Table 4. From the pressure distributions, one can see that low pressure is better distributed over the airfoil chord, and the peak of its minimum value is strongly reduced. This new load distribution results in different stall behaviors, as explained in the following sections. In the following, the term “flexible droop nose” will refer to the geometry described in this subsection, obtained by increasing both the camber and the thickness of the airfoil.

A numerical optimization and wind-tunnel tests of a flexible droop nose device combined with a Fowler flap are discussed in [16,17]. Table 5 reports a comparison of the results obtained with the present droop nose and these referenced data. It is seen that the gains in maximum lift coefficient and in the stall angle of attack are significantly larger for the present combination with the Coanda flap.

Table 2 Improvements achieved by increasing the thickness of a rigid nose deflected of 10 deg

	$C_{l_{max}}$	α_{stall} , deg
Droop nose $\beta = 10$ deg, $th_{1e} = 1.0$	5.64	6.3
Droop nose $\beta = 10$ deg, $th_{1e} = 1.6$	5.86	9.0

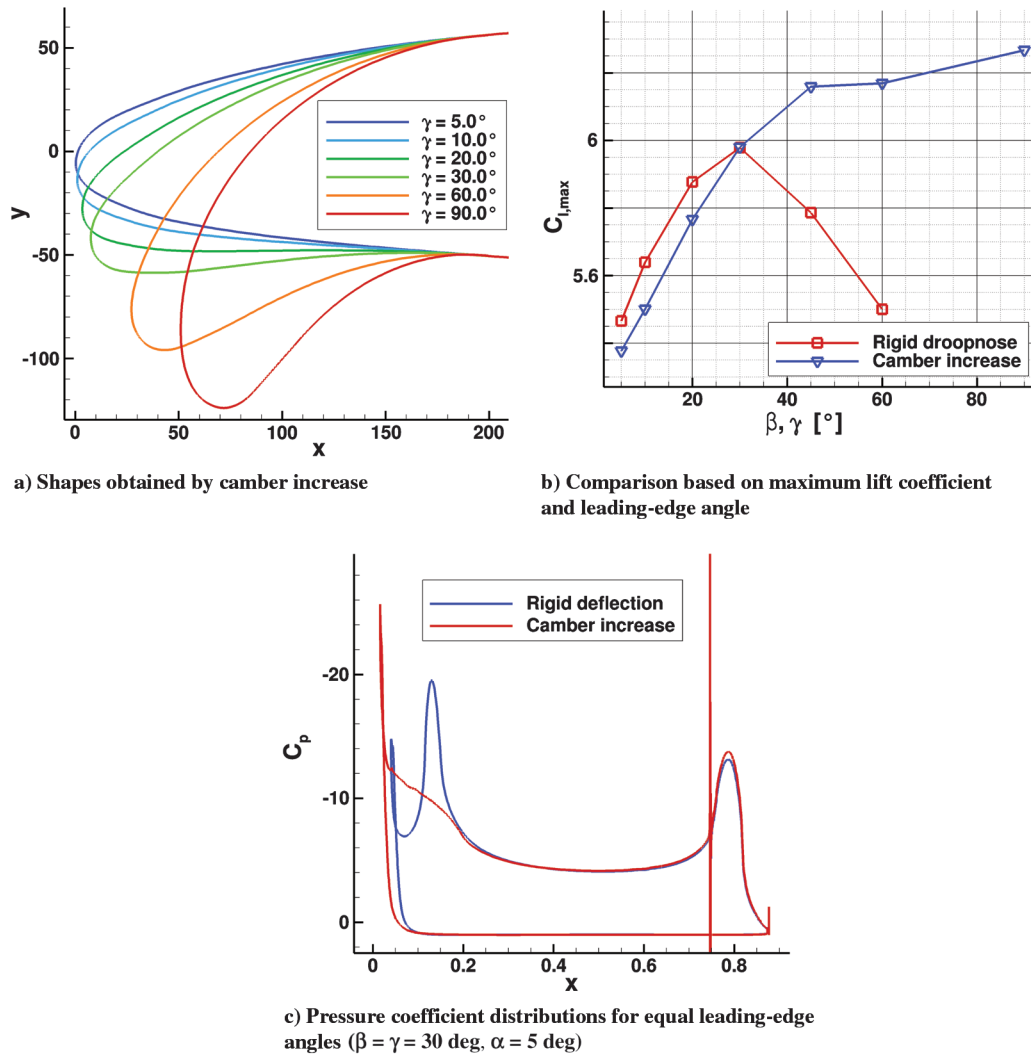


Fig. 6 Shapes of camber-increased noses and performance comparison to rigid droop nose ($Re = 10^7$, $M = 0.15$, $C_\mu = 0.06$).

V. Droop Nose and Clean-Nose Response to Variations of C_μ and α

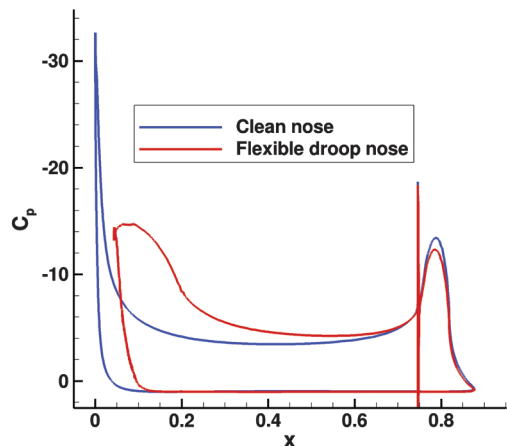
In this section, the clean-nose configuration and the droop nose obtained by increasing camber and thickness are analyzed for different blowing momentum, and their behaviors at high angles of attack are described. The flow phenomena that generate stall appear to be strongly affected by the leading-edge device. To thoroughly understand the different behaviors, it is worthwhile to investigate the most important flow quantities that govern the flow around the airfoil and their interaction.

Table 3 Improvements achieved by increasing the camber of the mean line to an angle at the leading edge of 90 deg

	$C_{l,max}$	α_{stall} , deg
Clean nose	5.27	1.5
Camber increase $\gamma = 90$ deg	6.267	15.0

Table 4 Improvements achieved by increasing the camber and the thickness of the nose

	$C_{l,max}$	α_{stall} , deg	$C_{d,stall}$	$C_{m,stall}$
Clean nose	5.27	1.5	0.0886	-2.184
Camber plus thickness increase	6.30	15.0	0.107	-2.44
Variations relative to clean nose	+19.5%	+13.5	+20.8%	-11.7%



As shown in Fig. 8a, the position of the wall jet is determined by two opposing effects. On one side, the jet is kept attached to the flap surface by the Coanda effect. On the other side, the inertia of the outer flow that results from the flow over the airfoil suction side upstream of the blowing slot causes the jet to slow down and possibly separate from the wall. This last phenomenon is affected by the characteristics of the outer flow upstream of the slot. As its boundary-layer momentum thickness increases, the outer flow progressively

Table 5 Aerodynamic improvements yielded by a flexible droop nose in combination with different high-lift flaps

	Coanda flap (present analysis, $C_\mu = 0.06$)	Fowler flap [16] (2-D CFD)	Fowler flap [17] (2-D experiments)
$\Delta C_{l_{max}}$	1.01	0.7	0.4
$\Delta \alpha_{stall}$, deg	13.75	5.5	5.5

separates from the jet that, as a consequence, stays closer to the flap surface. It appears that the flow dynamics over the flap are dependent on the following factors:

1) The first factor is the jet momentum coefficient. The momentum coefficient of the jet affects both the Coanda effect and the mixing between the jet and the outer flow. In the following, it is explained how these two effects are balanced in relation to the nose shape, the angle of attack, and C_μ .

2) The second factor is flow over the slot. The characteristics of the flow that is mixed with the jet are fundamental to ensure the efficiency of the active high-lift flap. The flow upstream of the slot is the result of the leading-edge behavior, and this is affected by the angle of attack and the jet momentum coefficient.

3) The third factor is the angle of attack. Downstream of the slot, the wake of the outer flow boundary layer receives jet momentum by turbulent transport. This is needed to overcome the positive pressure gradient, which is determined by the angle of attack.

The reaction of the flowfield to variations of C_μ and α is described in the following sections by means of boundary-layer velocity profiles and integral thickness parameters. These are extracted at two locations: over the slot, and near the trailing edge (Fig. 8b).

In Fig. 9a, the momentum thickness of the boundary layer is displayed close to the flap trailing edge. An increase of jet momentum coefficient improves the Coanda effect, which keeps the jet closer to the wall, thereby reducing the boundary-layer momentum thickness at the trailing edge. An increase of α involves a higher positive pressure gradient along the suction side of the airfoil, which increases the momentum thickness upstream of the slot (Fig. 9b). As a result, a progressive separation occurs between the flow and the jet, which allows the jet to flow closer to the wall. In the following, examples of this phenomenon are presented.

For outer flow attachment, the shape of the nose is of primary importance, as it affects the flow that reaches the jet. Figure 10 shows how the velocity profile of the boundary layer over the slot depends on C_μ . With both geometries, a higher blowing rate creates a higher edge velocity. In Fig. 9b, the momentum thickness of the boundary layer in this area is plotted. In both cases, the angle of attack has a strong influence on increasing the boundary-layer thickness. However, the clean-nose configuration appears to be much more sensitive to jet momentum variations. This plays a key role in the stall behavior of the two configurations, as explained in the following.

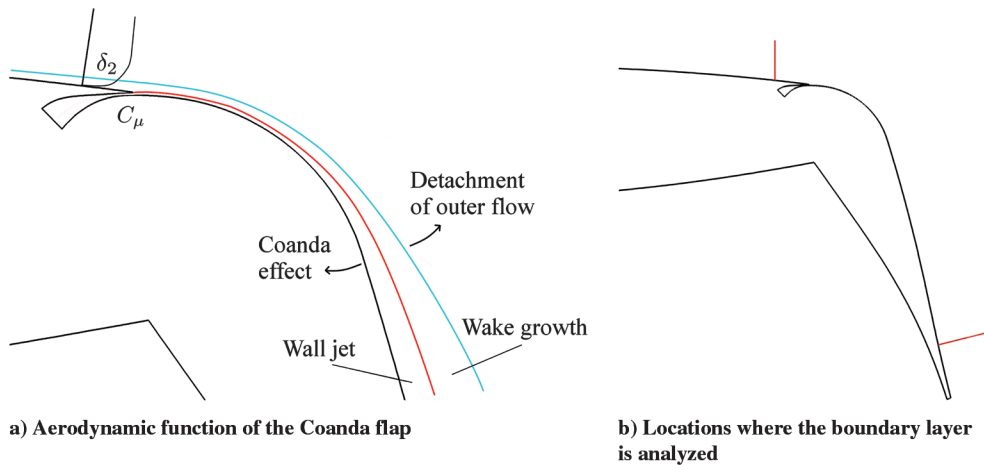


Fig. 8 References for the flowfield analysis.

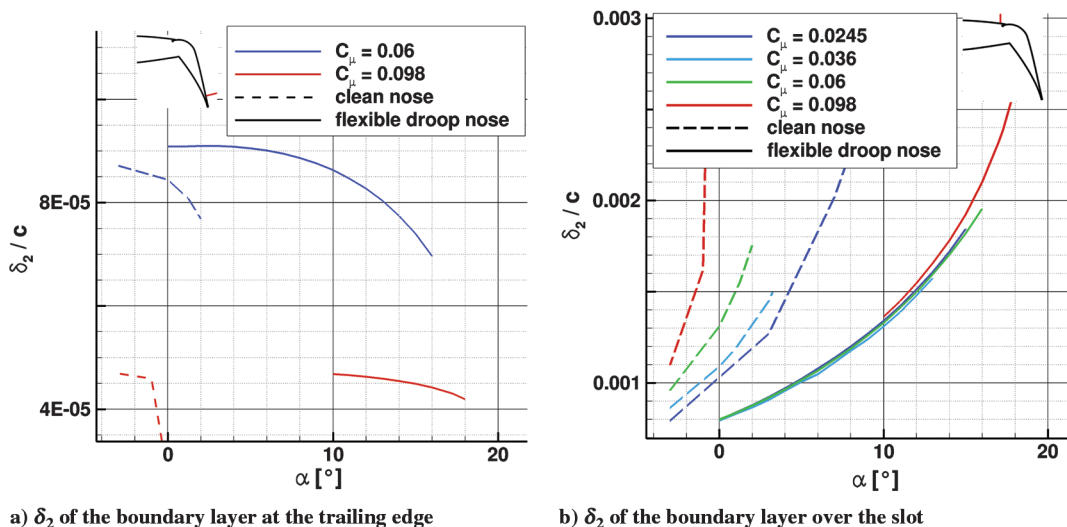


Fig. 9 Momentum thickness of the boundary layer in the two locations, for different C_μ and α .

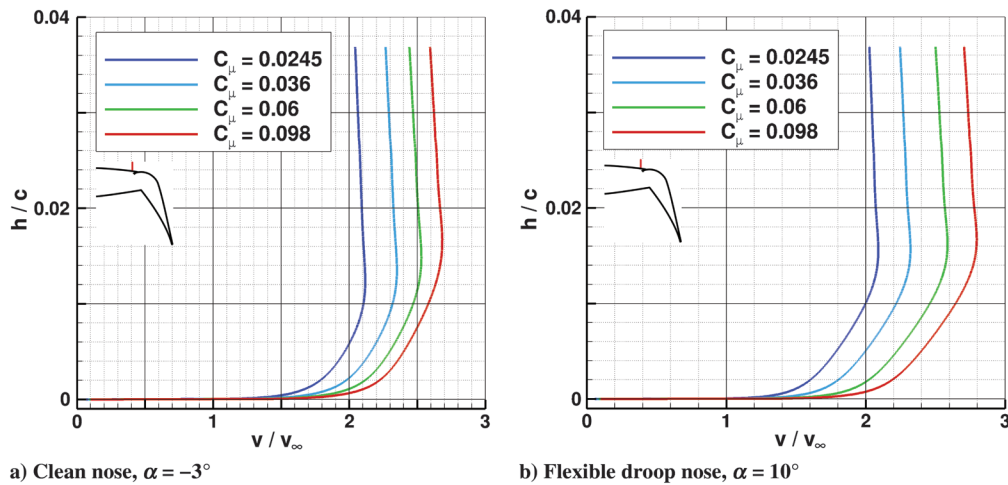


Fig. 10 Velocity profiles over the blowing slot, at constant angles of attack.

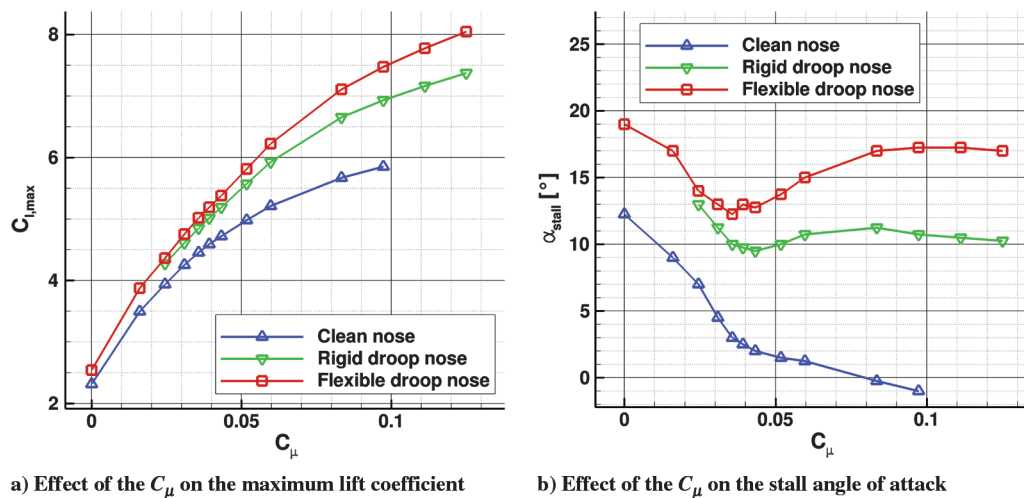


Fig. 11 Response of the two airfoils to different momentum coefficients ($\delta = 65^\circ$).

A. Overall Stall Behaviors

Based on the boundary-layer analysis as previously described, it is possible to explain the stall behaviors of the different leading-edge configurations. Figure 11 shows the responses to different jet momentum, in terms of maximum lift coefficient and stall angle of attack, of the clean nose, rigid droop nose, and flexible droop nose. From a technical point of view, the rigid droop nose is a less complex solution than the flexible droop nose. For this reason, it is included in the comparison. It is seen that the rigid droop nose yields a somewhat smaller performance improvement compared to the flexible droop nose. Therefore, only the flexible droop nose is compared with the clean nose in the following analyses of the flow phenomena.

Note that the values corresponding to the no-blowing conditions are considered less accurate than the other cases because of the large separation area that occurs downstream of the 65-deg-deflected flap. These regions are characterized by unsteady, vortical flow phenomena, which cannot be accurately captured with the Spalart-Allmaras RANS model.

1. Effect of C_μ on $C_{l,max}$

In Fig. 11a the increasing jet momentum involves an augmentation of circulation, which results in higher $C_{l,max}$. However, the efficiency of blowing decreases at high C_μ . For low momentum, the graph has a higher slope and describes the regime of “boundary-layer control.” Here, the wall jet is too weak to overcome the adverse pressure gradient of the flap until the trailing edge, causing the flow to separate from the flap. The separation point is delayed by increasing C_μ until the trailing edge is reached. At this condition, a second regime,

“supercirculation,” is initiated. The increase of C_l after this point is given by the jet effect on the streamlines downstream of the trailing edge. This explains the lower efficiency of this second region: in order to obtain the same improvement of C_l , a higher increase of blowing momentum is needed.

2. Effect of C_μ on Stall Angle of Attack

The stall angle of attack directly depends on the interaction between the flow at the leading edge and at the flap. As mentioned previously, the trailing-edge device increases the suction at the leading edge, which may induce leading-edge separation. This can be avoided by leading-edge protection that, in the present case, creates a different stall mechanism. This explains the different responses of the stall angle of attack to changes of C_μ in boundary-layer control and supercirculation regimes. A more detailed discussion about the stalling behaviors is presented in the next sections.

B. Stall Behavior in Boundary-Layer Control Regime

In this regime, the jet does not have sufficient momentum to keep the flow attached to the flap surface until the trailing edge. At low angles of attack, the jet separates from the wall, following the same path as the outer flow (Figs. 12a, 13a and 13b). As the angle of attack increases, both the positive pressure gradient over the flap and over the main part of the airfoil increase. The result of these effects is described in Fig. 14, which shows the velocity profile just before the separation point, at $C_\mu = 0.036$ for the flexible droop nose configuration. Until $\alpha = 8^\circ$, the positive pressure gradient increases the separation region; whereas for higher angles of attack,

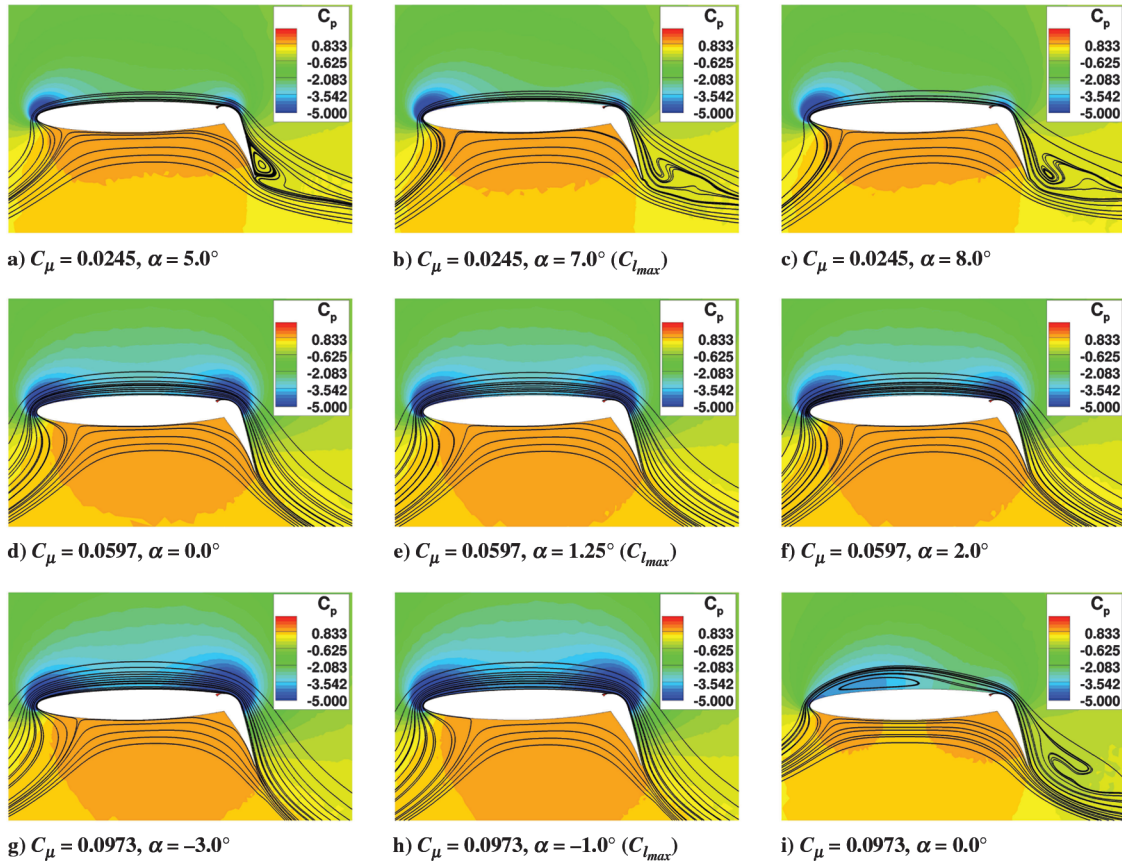


Fig. 12 Clean-nose configuration, C_p contour, and streamlines.

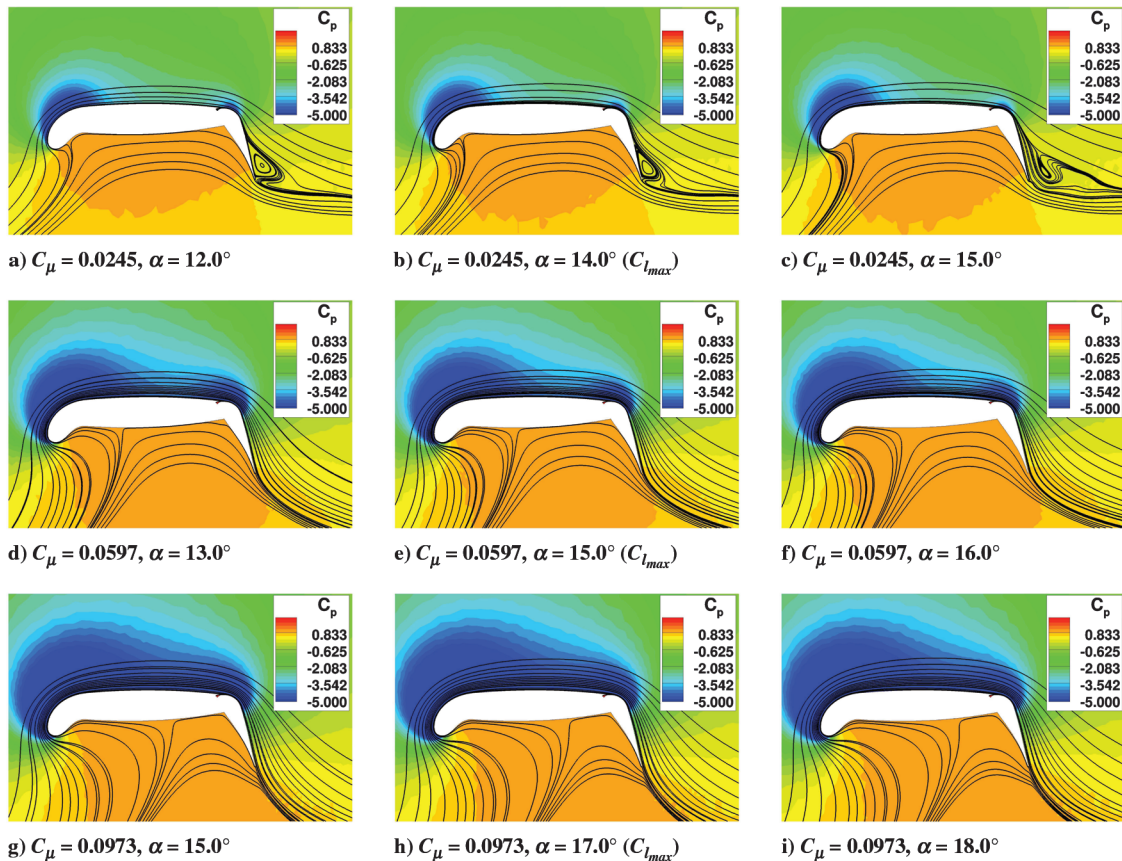


Fig. 13 Flexible droop nose configuration, C_p contour, and streamlines.

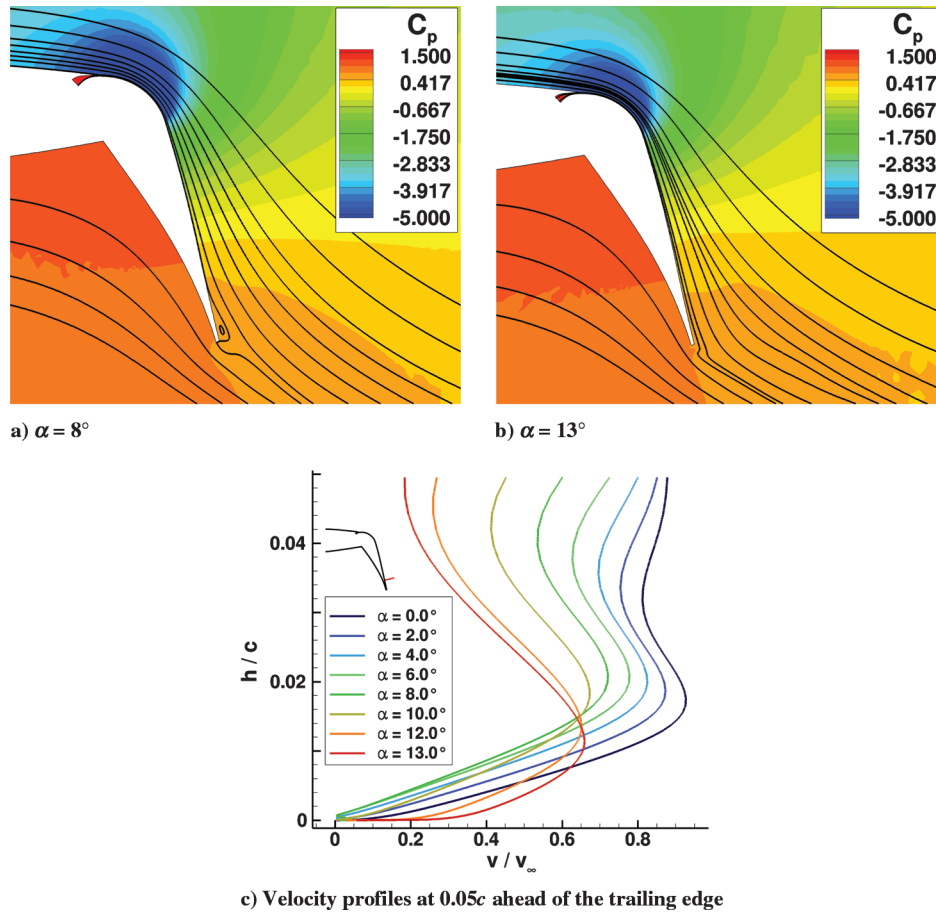


Fig. 14 Trailing-edge boundary-layer evolution for $C_\mu = 0.036$, flexible droop nose.

the suction at the leading edge, which increases the boundary-layer momentum thickness over the slot, becomes more important. As a consequence, the attachment between the jet and the outer flow decreases, leaving the jet to stay closer to the surface of the flap. This phenomenon can cause the separation to disappear, as seen in Figs. 14a and 14b. In some cases, a recirculation area occurs between the jet and the outer flow. This happens typically for low blowing rates; see Figs. 12b, 12c and 13c. Note that the very high losses at the leading edge caused by high C_μ with the clean-nose configuration can cause a similar flow topology; see Fig. 12i.

An increase of C_μ improves both the Coanda effect and the flow momentum transferred to the outer flow. As a result, the separation point is moved toward the trailing edge. This increases the lift coefficient but decreases the stall angle of attack. In more detail, since the separation occurs closer to the trailing edge, one observes higher suction peak levels at the nose for a given value of α . Therefore, the progressive separation between the jet and the outer flow begins at lower angles of attack; hence, α_{stall} decreases with increasing C_μ .

C. Stall Behavior in Supercirculation Regime

In the supercirculation regime, the jet has sufficient momentum to stay always attached to the flap surface. Therefore, the position of the jet remains constant, contrarily to the previous case (Figs. 12d–12i and 13d–13i). In this condition, the leading-edge configuration plays a more important role, as it affects the momentum losses of the outer

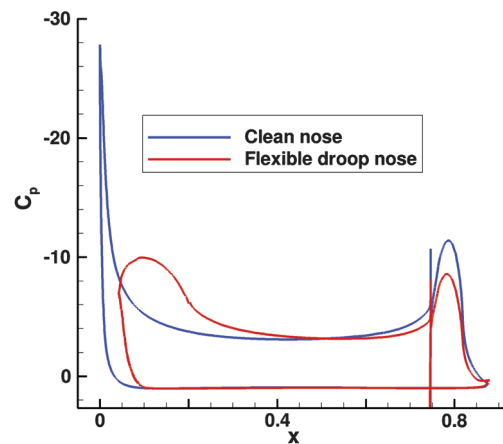


Fig. 15 C_p distributions corresponding to $C_l = 4.719$, $\alpha_{\text{droop}} = 12$ deg, $\alpha_{\text{clean}} = 2$ deg, $C_{\mu,\text{droop}} = 0.0309$, and $C_{\mu,\text{clean}} = 0.0433$.

flow upstream of the slot. As mentioned previously, the momentum of the outer flow has an important influence on the mixing between jet and outer flow itself. For both leading-edge configurations, an increase of C_μ increases the momentum transferred to the outer flow from the jet. However, as shown in Fig. 9b, in the case of the clean nose, the momentum losses caused by high C_μ at the leading edge are very large; therefore, stall occurs at lower angles of attack. On the contrary, for the flexible droop nose the momentum thickness of the boundary layer over the slot is almost independent of C_μ ; therefore, the outer flow will overcome higher positive pressure gradients thanks to the increased C_μ , and stall is delayed. This happens until C_μ reaches values around 0.08. Note that, at a 17 deg angle of attack, the wall jet leaves the trailing edge in a direction normal to the freestream, just at the maximum of lift.

Table 6 Aerodynamic coefficients for $C_l = 4.719$

	C_μ	α , deg	C_l	C_d	C_m
Clean nose	0.0433	2.0	4.719	0.0719	-0.808
Flexible droop nose	0.0309	12.0	4.719	0.0784	-0.677
Variations relative to clean nose	-28.6%	+10.0		+9.0%	+16.2%

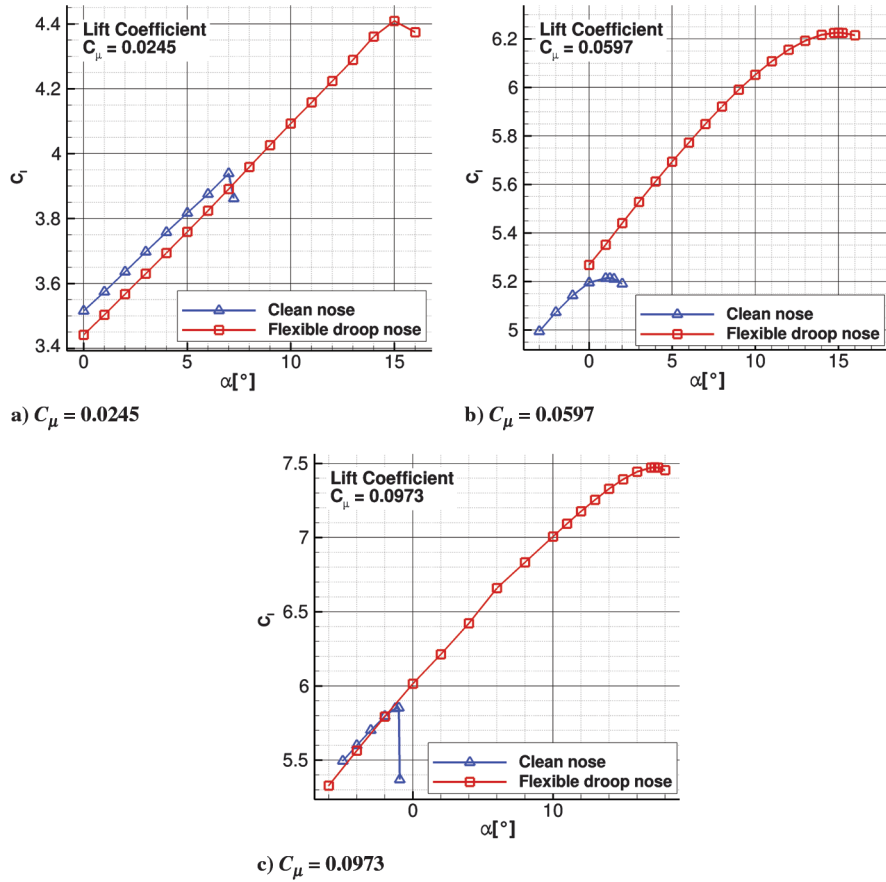


Fig. 16 Flexible droop nose effect on the lift coefficient.

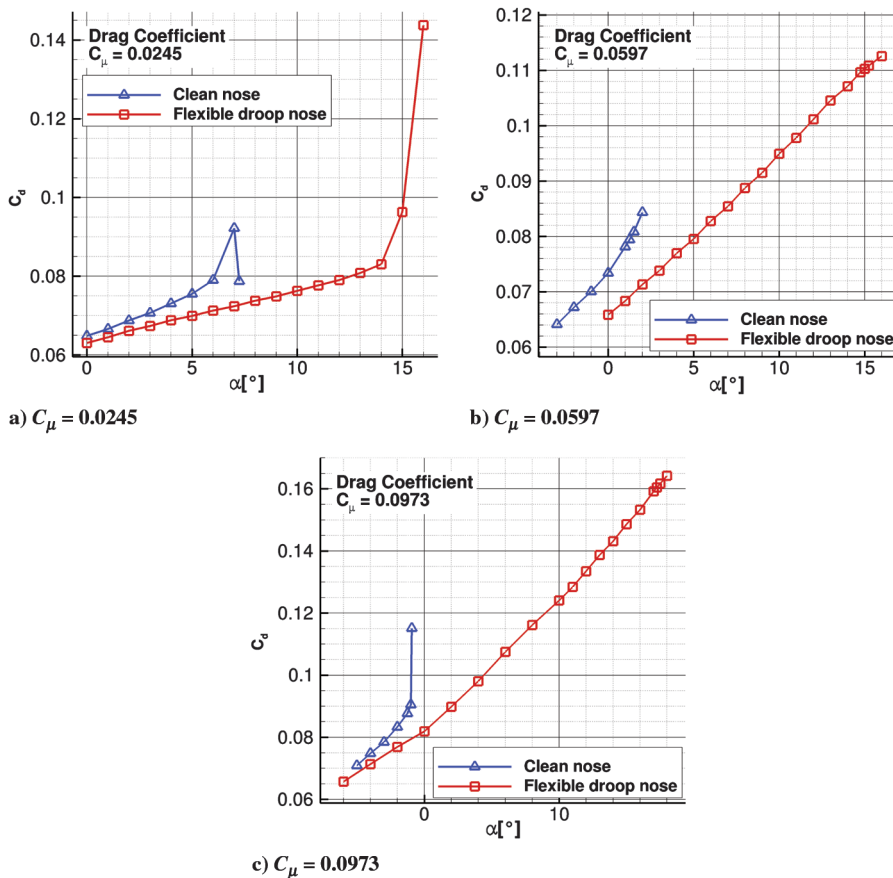


Fig. 17 Flexible droop nose effect on the drag coefficient.

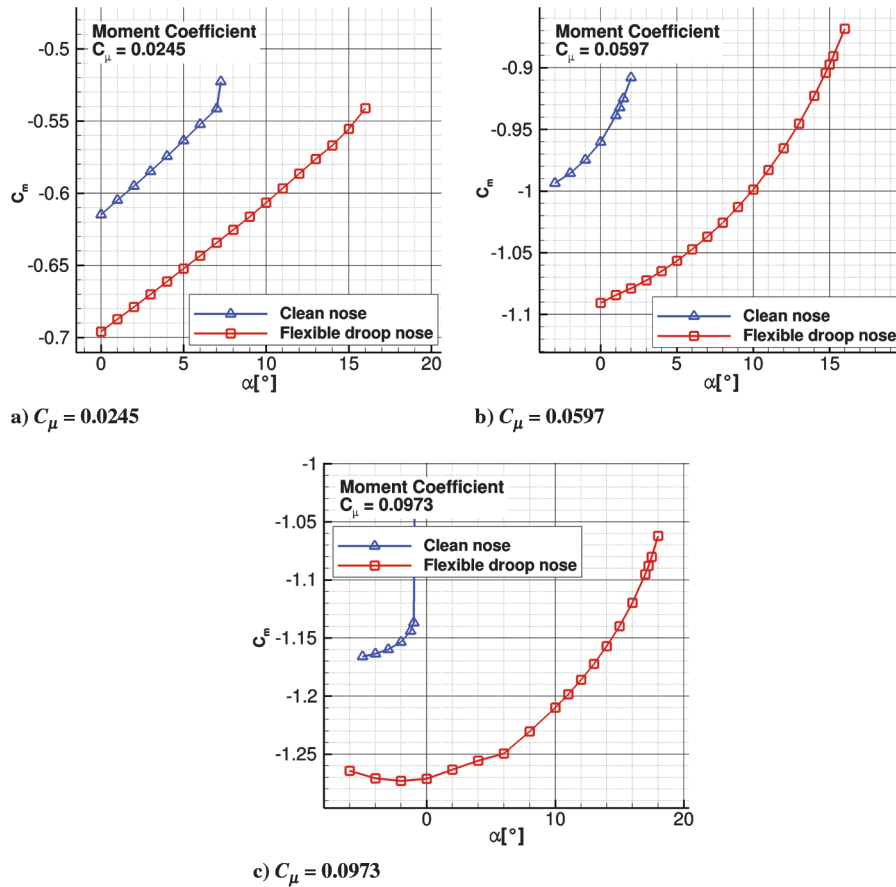


Fig. 18 Flexible droop nose effect on the moment coefficient.

D. Aerodynamic Coefficients

The capability of the flexible droop nose to reach higher angles of attack allows this geometry to achieve a target lift coefficient with a lower blowing rate. This is shown in Fig. 15, where the two configurations are compared for the same lift coefficient. The higher angle of attack along with the new curvature distribution of the upper surface raises the load on the front part of the airfoil. The reduced blowing momentum decreases the load on the Coanda surface. As a consequence, different aerodynamic coefficients are obtained, as shown in Table 6. Note that $C_l = 4.719$ is obtained by the clean configuration with $C_\mu = 0.0433$ at $\alpha = 2.0$ deg, which is the stall angle of attack. The same C_l is obtained by the flexible droop nose configuration with $C_\mu = 0.0309$ at $\alpha = 12.0$ deg, which is 1 deg before stall.

In Fig. 16, the lift curves of the two configurations are compared for different blowing rates. For low blowing rates, at the same C_μ and α , the lift generated with the flexible droop nose is slightly lower than for the clean nose. On the curves corresponding to $C_\mu = 0.0973$, one can also notice the effect of the different stall mechanisms that occur with high blowing rates: as explained in the previous subsection, the high circulation causes leading-edge separation for the clean nose, which results in an abrupt stall behavior.

Table 6 reports a higher drag coefficient in the case of flexible droop nose, due to the higher angle of attack. In Fig. 17, one can see that, for the same blowing rate and the same angle of attack, the flexible droop nose always yields lower drag.

An increase of angle of attack causes a progressive loading of the nose and unloading of the Coanda surface, which reduces the negative pitching moment, as shown in Fig. 18. The moment reference point is fixed for both geometries at 25% of the clean-nose chord. When the two airfoils generate the same lift, the absolute value of the pitching moment is somewhat lower in the case of the flexible droop nose, due to its specific pressure distribution (Fig. 15).

VI. Conclusions

New results on the combination of well-designed Coanda flaps and droop noses are presented. This combination brings a surprisingly large increase of maximum lift coefficient and stall angle of attack with respect to the configuration without leading-edge device. In particular, for C_μ higher than 0.036, these improvements appear to be larger than for the combination of a flexible droop nose with a conventional Fowler flap device. The effect of the flexible droop nose is to reduce the needed blowing power of the Coanda flap and to increase the angle of attack of the maximum lift coefficient. A target lift coefficient, $C_l \approx 4.7$, can be obtained with about 28% less jet momentum, which increases the lift gain factor by the same proportion. Moreover, the stall angle of attack is brought to values suitable for landing and takeoff operations: from 2 to 13 deg. Due to an improved load distribution along the chord, and the lower jet momentum, the absolute value of the pitching moment at the same lift coefficient is significantly reduced.

The analyses of stall mechanisms highlighted some important, unexpected phenomena: 1) progressive attachment of the Coanda jet to the flap for an increasing angle of attack; 2) separation between the Coanda jet and the outer flow in the case of low blowing rates, which creates a complex recirculation area between the two flow streams; and 3) flexible droop nose yielding increased stall angles of attack for large jet momentum coefficients.

The flow analysis also led to a more thorough understanding of the boundary-layer evolutions upstream of the slot and on the flap, which depend on the angle of attack and blowing rate. This knowledge will play an important role in the design of a closed-loop control for the blowing device, which is planned for the future development of the high-lift system. For this purpose, pressure and skin-friction sensors could be placed on the surface of the airfoil in critical areas, and their signals would be used to efficiently control the jet. The blowing rate would be, in this way, adapted to the current condition of the flow, leading to an overall reduction of the required blowing power.

It is noted that the presented flow simulations will have to be confirmed by the use of more advanced turbulence models, as well as by using experimental data. Future research of the Collaborative Research Center SFB880 will cover these directions.

Acknowledgments

The funding of this work of the Collaborative Research Center Sonderforschungsbereich 880 by the German Research Foundation (Deutsche Forschungsgemeinschaft) is thankfully acknowledged.

References

- [1] Katzmayr, R., "Wings with Nozzle Shaped Slots," NACA Translation TM 521, July 1929.
- [2] Nielsen, J. N., and Biggers, J. C., "Recent Progress in Circulation Control Aerodynamics," AIAA Paper 1987-001, 1987.
- [3] Yaros, S. F., "Synergistic Airframe-Propulsion Interactions and Integrations," NASA TM-1998-207644, 1998.
- [4] Englar, R. J., "Overview of Circulation Control Aerodynamics: Blown Force and Moment Augmentation and Modifications as Applied Primarily to Fixed Wing Aircraft," *Applications of Circulation Control Technology*, edited by Joslin, R. D., and Jones, G. S., Vol. 214, Progress in Astronautics and Aeronautics, AIAA, Reston, VA, 2006, pp. 37–99.
- [5] Jones, G. S., "Pneumatic Flap Performance for a Two-Dimensional Circulation Control Airfoil," *Applications of Circulation Control Technology*, edited by Joslin, R. D., and Jones, G. S., Vol. 214, Progress in Astronautics and Aeronautics, AIAA, Reston, VA, 2006, pp. 845–888.
- [6] Englar, R. J., and Hudson, G. G., "Development of Advanced Circulation Control Using High-Lift Airfoils," *Journal of Aircraft*, Vol. 21, No. 7, 1984, pp. 476–483. doi:10.2514/3.44996
- [7] Liu, Y., Sankar, L. N., Englar, R. J., Abuja, K. K., and Gaeta, R., "Computational Evaluation of Steady and Pulsed Jet Effects on a Circulation Control Airfoil," *Applications of Circulation Control Technology*, edited by Joslin, R. D., and Jones, G. S., Vol. 214, Progress in Astronautics and Aeronautics, AIAA, Reston, VA, 2006, pp. 557–577.
- [8] Jensch, C., Pfingsten, K. C., Radespiel, R., Schuermann, M., Haupt, M., and Bauss, S., "Design Aspects of a Gapless High-Lift System with Active Blowing," *Proceedings of Deutsches Luft- und Raumfahrtkongress*, Paper 121246, DGLR, Bonn, Germany, 2009.
- [9] Jensch, C., Pfingsten, K. C., and Radespiel, R., "Numerical Investigation of Leading Edge Blowing and Optimization of the Slot and Flap Geometry for a Circulation Control Airfoil," *Notes on Numerical Fluid Mechanics and Multidisciplinary Design*, Vol. 112, Springer-Verlag, New York, 2010, pp. 183–190.
- [10] Pflingsten, K. C., Jensch, C., Körber, K. V., and Radespiel, R., "Numerical Simulation of the Flow Around Circulation Control Airfoils," *Proceedings of 1st CEAS European Air and Space Conference*, Paper CEAS-2007-377, CEAS, Brussels, Belgium, 2007.
- [11] Pott-Pollenske, M., Alvarez-Gonzalez, J., and Dobrzynski, W., "Effect of Slat Gap on Farfield Radiated Noise and Correlation with Local Flow Characteristic," *9th AIAA/CEAS Aeroacoustics Conference*, AIAA Paper 2003-3228, 2003.
- [12] Shmilovich, A., and Yadlin, Y., "Flow Control for the Systematic Buildup of High Lift Systems," *3rd AIAA Flow Control Conference*, AIAA Paper 2006-2855, 2006.
- [13] Shmilovich, A., and Yadlin, Y., "Flow Control Techniques for Transport Aircraft," *AIAA Journal*, Vol. 49, No. 3, 2011, pp. 489–502. doi:10.2514/1.J050400
- [14] Ying, S. X., Spaid, F. W., McGinley, C. B., and Rumsey, C. L., "Investigation of Confluent Boundary Layers in High-Lift Flows," AIAA Paper 1998-2622, 1998.
- [15] Jirásek, A., and Amoinon, O., "Design of a High-Lift System with a Droop Nose Device," *Journal of Aircraft*, Vol. 46, No. 2, 2009, pp. 731–734. doi:10.2514/1.41520
- [16] Kintscher, M., Wiedemann, M., Monner, H. P., Heintze, O., and Kühn, T., "Design of a Smart Leading Edge Device for Low Speed Wind Tunnel Tests in the European Project SADE," *International Journal of Structural Integrity*, Vol. 2, No. 4, 2011, pp. 383–405. doi:10.1108/17579861111183911
- [17] Wild, J., "Experimental Investigation of Mach- and Reynolds-Number Dependencies of the Stall Behavior of 2-Element and 3-Element High-Lift Wing Sections," *50th AIAA Aerospace Sciences Meeting*, AIAA Paper 2012-108, 2012.
- [18] Englar, R. J., Smith, M. J., Kelley, S. M., and Rover, R. C., "Application of Circulation Control to Advanced Subsonic Transport Aircraft, Part I: Airfoil Development," *Journal of Aircraft*, Vol. 31, No. 5, Sept.–Oct. 1994, pp. 1160–1168. doi:10.2514/3.56907
- [19] Kroll, N., Rossow, C.-C., Schwamborn, D., Becker, K., and Heller, G., "MEGAFLOW—A Numerical Flow Simulation Tool for Transport Aircraft Design," *23rd ICAS Congress*, Paper 2002-1.10.5, ICAS, Bonn, Germany, 2002.
- [20] Schamborn, D., Gerhold, T., and Heinrich, R., "The DLR TAU-Code: Recent Applications in Research and Industry," *Proceedings of ECCOMAS CFD Conference [CD-ROM]*, Egmond aan Zee, The Netherlands, 2006.
- [21] Pflingsten, K. C., and Radespiel, R., "Experimental and Numerical Investigation of a Circulation Control Airfoil," *47th AIAA Aerospace Sciences Meeting*, AIAA Paper 2009-533, 2009.
- [22] Pflingsten, K. C., Cecora, R. D., and Radespiel, R., "An Experimental Investigation of a Gapless High-Lift System Using Circulation Control," *Proceedings of Katenet II Conference [CD-ROM]*, Bremen, 2009.
- [23] Shur, M. L., Strelets, M. K., Travin, A. K., and Spalart, P. R., "Turbulence Modeling in Rotating and Curved Channels: Assessing the Spalart–Shur Correction," *AIAA Journal*, Vol. 38, No. 5, 2000, pp. 784–792. doi:10.2514/2.1058
- [24] Richardson, L. F., "The Deferred Approach to the Limit," *Philosophical Transactions of the Royal Society of London, Series A: Mathematical and Physical Sciences*, Vol. 226, Nos. 636–646, 1927, pp. 299–361. doi:10.1098/rsta.1927.0008
- [25] Raymer, D. P., *Aircraft Design: A Conceptual Approach*, AIAA Education Series, AIAA, Reston, VA, 1999, p. 340.